Electronic Raman scattering in YBCO and other superconducting cuprates

T. Strohm and M. Cardona
Max-Planck-Institut für Festkörperforschung, Heisenbergstr. 1, D-70569 Stuttgart, Germany
(July 9, 2004)

Superconductivity induced structures in the electronic Raman spectra of high-T_c superconductors are computed using the results of *ab initio* LDA-LMTO three-dimensional band structure calculations via numerical integrations of the mass fluctuations, either in the whole 3D Brillouin zone or limiting the integrations to the Fermi surface. The results of both calculations are rather similar, the Brillouin zone integration yielding additional weak structures related to the extended van Hove singularities. Similar calculations have been performed for the normal state of these high-T_c cuprates. Polarization configurations have been investigated and the results have been compared to experimental spectra. The assumption of a simple $d_{x^2-y^2}$-like gap function allows us to explain a number of experimental features but is hard to reconcile with the relative positions of the A_{1g} and B_{1g} peaks.

I. INTRODUCTION

After ten years of research in the field of high-T_c superconductors[1] (HTSC), many of their properties have not yet been understood. In particular, the symmetry of the superconducting gap[2–4] is still controversial. Usually, one assumes that the superconducting condensate in the HTSC can be described by an order parameter $\Delta_{\mathbf{k}}$, which depends only on the quasi momentum $\mathbf{k}$, but not on band index n. Retardation effects are also often neglected, i.e. the gap is assumed to be independent of the frequency ω.

A wide range of experimental techniques can be employed to investigate the properties of the gap function. Among these, Raman scattering has played an important role.[5,6] The dependence of the Raman response on the directions of polarization of the incident and scattered light yields several independent spectra which provide a considerable number of constraints on the assumed $\mathbf{k}$-dependence of the gap function $\Delta_{\mathbf{k}}$. However, Raman scattering is not sensitive to the phase of the gap.

The Raman spectra at temperatures below T_c shows, in most HTSC, a clear gap-like structure which lies in the energy range of the optical phonons at the Γ point. These phonons have been identified for most HTSC,[7] and the subtraction of the corresponding structures from the spectra has become a standard procedure to isolate electronic structures containing gap information. Electronic Raman scattering spectra are now available for many high-T_c materials and, since they exhibit similar general features, most of these data are considered to be reliable. In this paper, we attempt to interpret these spectra from a theoretical point of view based on the full 3D one-electron band structure. We pay attention to both, line shapes and *absolute* scattering efficiencies.

The theory of electronic Raman scattering in superconductors was pioneered by Abrikosov and coworkers in two important papers.[8,9] In the first, they developed a theory for the scattering efficiency of *isotropic* Fermi liquids under the assumption that the attractive interaction between quasiparticles can be neglected. In the second paper, they extended this approach to anisotropic systems, introduced the effective mass vertex concept, and included Coulomb screening. The current form of the theory, developed mainly by Klein *et al.*,[10] takes into account the attractive pairing interaction and emphasizes the role of gauge invariance as well as the polarization dependence for anisotropic gaps. In order to compare the theoretical predictions with the experiment, we evaluate them numerically in a quantitative manner (including *absolute* scattering efficiencies!) and compare them to the experimental findings.

Several calculations of the electronic Raman scattering efficiency of HTSC have already been published. Some of them use highly simplified 2D band structures and a decomposition of the Raman vertex $\gamma_{\mathbf{k}}$ in Fermi surface (FS) harmonics[11] or Brillouin zone (BZ) harmonics, as well as FS integrations instead of the required BZ integrations.[5,12,13] The results of these calculations depend very strongly on the number of expansion coefficients used for $\gamma_{\mathbf{k}}$ and their relative values. Another approach[14] involves the use of band structures calculated in the framework of the local density approximation[15] (LDA) using the LMTO method.[16,17] Within the approximations of the LDA, this Raman vertex is exact, i.e. the only errors made in such a calculation arise from limitations of the LDA method itself and from the discretization of the Brillouin zone or Fermi surface. Some of these calculations, however, suffer from the fact that only the imaginary part of the Tsuneto function[18] has been used, and that only 2D integrations were performed.[6]

The present approach[19] is based on the full 3D LDA-LMTO band structure. It uses a BZ integration, screen-

ing effects are included, and both the real and imaginary part of the Tsuneto function are used as required by the theory. Electronic Raman spectra are calculated for $YBa_2Cu_3O_7$ (Y-123) and $YBa_2Cu_4O_8$ (Y-124). The orthorhombicity of the cuprates is also taken into account in the Raman vertex since we use as starting point the band structure of the *orthorhombic* materials.

The cuprates under consideration are not only of interest because of their superconducting, but also of their strange normal-conducting properties. Usual metals should show peaks in their Raman spectra at their plasma frequencies corresponding to Raman shifts of a few eV. The optimally doped cuprates, in contrast, show a very broad electronic background (from 0 to about 1 eV Raman shift), which is almost independent of temperature and frequency. The spectra of the underdoped HTSC, such as Y-124, show some temperature dependence at low frequencies ($\hbar\omega \ll kT$). It is possible to explain these peculiarities, together with other properties, by assuming a certain form of the quasiparticle lifetime, as was done in the Marginal Fermi Liquid theory.[20,21]

For the superconducting state, various forms for the gap function have been proposed. That which has received most experimental support has $d_{x^2-y^2}$ symmetry, i.e., B_{1g} symmetry in tetragonal HTSC. The power of Raman scattering to confirm such gap function has been questioned, because, among other difficulties to be discussed below, it only probes the *absolute* value of the gap function, i.e. it cannot distinguish between a $d_{x^2-y^2}$-like gap function (for instance $\cos 2\phi$), and a $|\cos 2\phi|$ gap function, which corresponds to anisotropic s (A_{1g}) symmetry. However, it was pointed out that addition of impurities can be used to effect the distinction.[22]

This paper is organized as follows: in Sec. II, we review the main properties of the band structures of the investigated cuprates, as obtained by LDA-LMTO calculations. Sec. III discusses the theory of electronic Raman scattering in systems with an anisotropic band structure. We first introduce the basic concept of Raman vertex, and then present an expression relating the scattering efficiency to the Raman susceptibility. In Sec. IV and V we derive expressions for the Raman susceptibility in the superconducting and normal conducting phases, and discuss some effects not directly contained in the presented form of the theory. Section VI is concerned with aspects of the experiments which have to be taken care of, especially with regard to the comparison with the theory. Finally, in Sec. VII the results of our numerical calculation are presented and compared to the experimental results. The difference between calculations involving only FS averaging, and those in which such averaging is performed over the whole BZ, are discussed.

II. LDA BAND STRUCTURE

The basis of our calculation is the LDA-LMTO band structure of the HTSC under consideration.[17] For the sake of further discussion, we shall describe briefly such band structure.

The Fermi surface of $YBa_2Cu_3O_7$ (Y-123)[17] consists of four sheets, an even and an odd $pd\sigma$-like plane band, a $pd\sigma$-like chain sheet and a very small $pd\pi$-like chain sheet. The latter is predicted by the full-potential LMTO calculations as well as LAPW calculations.[23] We use the atomic spheres approximation (ASA) to the LMTO, which does not reproduce this rather small feature. In the case of Y-123 the three $pd\sigma$-like conduction bands extend from -1 eV to 2 eV relative to the Fermi energy. They are embedded in a broad valence band, which ranges from -7 eV to 2 eV and consists of 36 bands (mainly Cu-d and O-p orbitals). Below -7 eV, there is a gap of 4 eV. Above the conduction band, there is another gap of 0.5 eV, above which are the lowest fully unoccupied bands which consist mainly of d orbitals of Y and Ba.

The band structure of $YBa_2Cu_4O_8$ (Y-124) shows similar features. There is an additional $pd\sigma$-like chain band, while the $pd\pi$-like chain bands are predicted by both, full-potential LMTO and LAPW to contain no holes, i.e. to be completely filled.

An interesting feature of the band structure of both Y-123 and Y-124 is an extended saddle point[16] on the k_x-axis near the X point. This extended saddle point corresponds to a van Hove singularity at approximately 25 meV (Y-123) and 110 meV (Y-124), respectively, below the Fermi level. As will be shown, the comparatively large density of states in this energy region and the warped nature of the corresponding bands has an influence on the calculated electronic Raman spectrum.

The band structure which we used in our numerical calculations was evaluated for Y-123 on a mesh of $48\times48\times12$ points in the first BZ, involving 4373 irreducible points. The band structure of Y-124 is less sensitive to the resolution of the grid (because the extended saddle point lies deeper with respect to the Fermi surface). It was thus sufficient to use a $24 \times 24 \times 12$ mesh with 1099 irreducible points. The calculations of the self-consistent potential have been performed in the ASA. Therefore, the $pd\pi$ chain band around the S point, which should be partly filled, is completely filled. Because of the small number of states involved, we do not think this should affect significantly our results.

As stressed above, our calculations are based on a band structure obtained within the LDA. We are aware of the fact, that the mean free path for transport in the direction of the c-axis is smaller than the size of the unit cell, i.e. that a description by means of a band structure $\epsilon_{n\mathbf{k}}$ may be questionable (Ioffe-Regel-limit). Nevertheless a nontrivial band structure in the c-direction may simulate some of the c-direction confinement effects and represent, after integration along k_z, a reasonable 2D band struc-

ture.

III. GENERAL THEORY

Two approaches have been used to derive the cross section (called scattering efficiency when referred to unit path length in the solid) of electronic Raman scattering in superconductors with anisotropic Fermi surfaces. The first uses Green's functions,[8–10,24] and the second the kinetic equation.[25,5] Both start with the simplification of the Hamiltonian, using $\mathbf{k}\cdot\mathbf{p}$ theory, which relates the Raman vertex $\gamma_{\mathbf{k}}$ to the inverse effective mass tensor.[9] We first briefly review this procedure and, subsequently, the derivation of the expression for the scattering efficiency using the diagrammatic approach.

A. The Raman vertex

To derive an expression for the efficiency for electronic Raman scattering, one has to replace the momentum $\mathbf{p}$ in the Hamiltonian by $\mathbf{p}-(e/c)\mathbf{A}$. This yields two distinct perturbation terms: $H_{AA}=(r_0/2)\mathbf{A}^2$, quadratic in the vector potential, and $H_A=-(e/mc)\mathbf{A}\cdot\mathbf{p}$, linear in A (we use the transverse gauge; $r_0=e^2/(m_0c^2)$ denotes the classical electron radius). The relevant states in the theory are composed of the state of electrons in the sample plus the state of the photon field. The initial state of the photon field has n_L laser photons with wave vector $\mathbf{k}_L$ and polarization $\mathbf{e}_L$ and $n_S=0$ scattered photons with wave vector $\mathbf{k}_S$ and polarization $\mathbf{e}_S$. The final state has one laser photon less but one scattered photon (Stokes scattering). The vector field can thus be written as a superposition of an incoming and a scattered plane wave, $\mathbf{A}=\mathbf{A}_L+\mathbf{A}_S$ with

$$\mathbf{A}_S=A_S^+\mathbf{e}_S^* e^{-i\mathbf{k}_S r}\ , \qquad \mathbf{A}_L=A_L^-\mathbf{e}_L e^{i\mathbf{k}_L r}\ , \tag{1}$$

where A_S^+ contains the creation operator for the scattered photon and A_L^- the annihilation operator for the laser photons (note that these are not hermitian).

Since Raman scattering is a second order process in $\mathbf{A}$, the term H_{AA} has to be treated in first order perturbation theory. It is therefore nonresonant and includes only intraband scattering. The matrix elements are given by

$$\begin{aligned} M^{(1)}_{n_f n_i}(\mathbf{q},\mathbf{k}) &= \frac{1}{2} r_0 \left\langle n_f\mathbf{k}+\mathbf{q} \mid \mathbf{A}^2 \mid n_i\mathbf{k}\right\rangle \\ &= r_0\big\langle A_S^+A_L\big\rangle \mathbf{e}_S^*\mathbf{e}_L\delta_{n_i n_f}\ , \end{aligned} \tag{2}$$

whereas $\big\langle A_S^+A_L\big\rangle$ denotes a matrix element involving the initial and final state of the photon field and $\mathbf{q}=\mathbf{k}_L-\mathbf{k}_S$ is the momentum transfer from the photon field to the sample. For other values of $\mathbf{q}$, the matrix element (2) vanishes.

The second term, H_A, produces resonances via second order perturbation theory. It has the form

$$M^{(2)}_{n_f n_i}(\mathbf{q},\mathbf{k}) = r_0\big\langle A_S^+A_L\big\rangle \sum_{n_m}\Gamma^{(2)}_{n_f n_i;n_m}(\mathbf{q},\mathbf{k}) \tag{3}$$

with the expression

$$\Gamma^{(2)}_{n_f n_i;n_m}(\mathbf{q},\mathbf{k}) = \tag{4}$$

$$\frac{\langle n_f\mathbf{k}+\mathbf{q} \mid \mathbf{e}_S^*\mathbf{p} \mid n_m\mathbf{k}+\mathbf{k}_L\rangle\,\langle n_m\mathbf{k}+\mathbf{k}_L \mid \mathbf{e}_L\mathbf{p} \mid n_i\mathbf{k}\rangle}{\epsilon_{n_i\mathbf{k}}-\epsilon_{n_m\mathbf{k}+\mathbf{k}_L}+\omega_L+i0} + \\ + \frac{\langle n_f\mathbf{k}+\mathbf{q} \mid \mathbf{e}_L\mathbf{p} \mid n_m\mathbf{k}-\mathbf{k}_S\rangle\,\langle n_m\mathbf{k}-\mathbf{k}_S \mid \mathbf{e}_S^*\mathbf{p} \mid n_i\mathbf{k}\rangle}{\epsilon_{n_i\mathbf{k}}-\epsilon_{n_m\mathbf{k}-\mathbf{k}_S}-\omega_S+i0}\ .$$

Here, ω_L and ω_S are the frequency of the incoming and scattered light, respectively. Note that the states in the sum above are states of the sample only. We have used Bloch states with band and crystal momentum indices. The wavevectors of light, $\mathbf{k}_L$ and $\mathbf{k}_S$, can usually be neglected in the matrix elements of Eq. (4) because $v_F\ll c$. For the same reason, $\epsilon_{n_m,\mathbf{k}+\mathbf{k}_L}\approx\epsilon_{n_m,\mathbf{k}}$. Therefore, we introduce the symbol $\Gamma^{(2)}_{n_f n_i;n_m}(\mathbf{k})$ to denote expression (4) with the light wavevectors set equal to zero.

If we now add the contributions of both terms in Eqs. (2) and (3) and introduce second quantization, we are left with the *effective Hamiltonian*

$$H_R = r_0\big\langle A_S^+A_L\big\rangle\,\tilde{\rho}_{\mathbf{q}} \tag{5}$$

as perturbation Hamiltonian leading to Raman scattering. The effective density operator $\tilde{\rho}_{\mathbf{q}}$ can be expressed in the form

$$\tilde{\rho}_{\mathbf{q}} = \sum_{n_f,n_i,\mathbf{k}} \gamma_{n_f n_i}(\mathbf{k})\, c^+_{n_f,\mathbf{k}+\mathbf{q}} c_{n_i,\mathbf{k}}\ . \tag{6}$$

using fermionic creation and annihilation operators for Bloch electrons as well as the nondiagonal Raman vertex

$$\gamma_{n_f n_i}(\mathbf{k}) = \mathbf{e}_S^*\mathbf{e}_L\delta_{n_f n_i} + \sum_{n_m}\Gamma^{(2)}_{n_f n_i;n_m}(\mathbf{k})\ . \tag{7}$$

If we are interested mainly in the low frequency region, say Raman shifts below 50 meV, no *real* interband transitions of significant weight are possible. This can easily be seen from the band structure (Fig. 2 of Ref. 16). Therefore, we introduce the (intraband) *Raman vertex* $\gamma_n(\mathbf{k})=\gamma_{nn}(\mathbf{k})$.

We proceed by discussing a very important simplification of (4) (with $n_i=n_f=n$ and $\mathbf{q}=0$), the *effective mass approximation*. Four different cases will be discussed. First, the virtual intraband transition with $n_m=n_i$. In this case, up to first order in v_F/c, we have $\langle n_m\mathbf{k}\mid\mathbf{p}\mid n_i\mathbf{k}\rangle=\langle n_i\mathbf{k}\mid\mathbf{p}\mid n_m\mathbf{k}\rangle$ (remember that $n_i=n_f$) and $\epsilon_{n_i\mathbf{k}}-\epsilon_{n_m\mathbf{k}}=0$. Then, it can be seen that the contributions of virtual *intra*band transitions relative to the contribution of virtual *inter*band transitions to intermediate states are of the order of the Raman shift over the laser frequency, i.e. $\omega/\omega_L\ll 1$, and can therefore be neglected. The second case are the virtual *inter*band

transitions involving bands which are much farther away from the FS than the light frequency. Then, because of $|\epsilon_{n_i} - \epsilon_{n_m}| \gg \omega_L$, the light frequencies ω_L as well as ω_S can be neglected in (4). The third case also involves virtual interband transitions, but for bands at about the laser frequency above the Fermi surface. Here, the scattering is resonant, and the spectra are expected to depend strongly on the laser wavelength. One can try to avoid this situation by using different laser lines. So we assume that in the third case ω_L and ω_S also can be neglected. Finally, the forth case consists of virtual interband transitions to neighboring bands with $\Delta\epsilon \ll \omega_L$. In this case, neglecting ω_L and ω_S is more difficult to justify. We do it nevertheless and reach the approximate conclusion that we can neglect the light frequencies in Eq. (4) and can restrict the sum in (3) to all $n_m \neq n_i$. Then, Eq. (7) becomes completely equivalent to the expression for the inverse effective mass from $\mathbf{k}\cdot\mathbf{p}$ theory and we can write

$$\gamma_n(\mathbf{k}) = \frac{m}{\hbar^2}\sum_{i,j} \mathbf{e}^*_{S,i}\frac{\partial^2\epsilon_{n\mathbf{k}}}{\partial k_i \partial k_j}\mathbf{e}_{L,j} \tag{8}$$

i.e. the Raman vertex is equal to the inverse effective mass contracted with the polarization vectors of the laser light and the scattered light, respectively.

Therefore, using the term H_R with the intraband Raman vertex $\gamma_{n\mathbf{k}} = \gamma_{nn}(\mathbf{k})$ in Eq. (6) as perturbation to the Hamiltonian for $\mathbf{A} = 0$ and treating this in first order perturbation theory is, under the mentioned restrictions, equivalent to taking into consideration both terms H_A and H_{AA}.[9]

According to the LMTO calculations, for Y-123 and Y-124 there are bands above a band gap between approximately 2 eV and 2.5 eV above the Fermi energy. These bands can present a problem with respect to the former discussion, because they are almost resonant for typical laser wavelengths like 514.5 nm. The same is true for the conduction bands, which extend until 2 eV above the Fermi surface. Note that due to the strong on-site interaction at the Cu-d orbitals, correlation effects are expected to be important in the electronic structure. It is possible that at energies of the order of 1 eV or more above the Fermi surface the picture of the Hubbard bands is a better description of the band structure and may explain the weak dependence of the Raman spectra on the laser frequency observed for laser frequencies in the visible range. The band structure shows many bands at about the laser frequency below the Fermi energy. These should yield resonant contributions to the Raman efficiency.

Because the Raman vertex $\gamma_{\mathbf{k}}$ is, in the given approximation, the second derivative of the energy with respect to $\mathbf{k}$, the A_{2g} component for tetragonal crystals vanishes in this version of the theory (A_{2g} is the symmetry of an antisymmetric tensor). If one considers once more the effects of a nearby resonance, it can be easily seen that the Raman tensor does not have to be symmetric. This stresses again the questionability of the effective mass approach if the scattering is resonant.

B. The scattering efficiency

Using the effective mass approach, we arrived at the effective Hamiltonian (5) with the effective mass determining the Raman vertex. This effective Hamiltonian is linear in $\mathbf{A}_L \cdot \mathbf{A}_S$. The derivation of the scattering efficiency using linear response theory is now a straightforward task.

The first step is finding a relation between the Raman efficiency and a dynamical structure factor of the sample. Then, in a next step, the fluctuation-dissipation theorem is used to connect the dynamical structure factor to the imaginary part of a susceptibility, in our case the *Raman susceptibility*.

To establish the relation to the dynamical structure factor, we add the time evolution factor $e^{-i\omega t}$ to the effective Hamiltonian (5) and use the golden rule to find the transition rate from a state i to a state f of the sample. Then, we sum over all final states f of the sample and do a thermal averaging over the initial states i. The transition rate from a state with $n_L \equiv n_{\mathbf{k}_L\mathbf{e}_L}$ laser photons and no scattered photon to a state with $n_L - 1$ laser photons and $n_S \equiv n_{\mathbf{k}_S\mathbf{e}_S} = 1$ scattered photon at a temperature T is given by the expression

$$\Gamma^T(\mathbf{k}_L, \mathbf{e}_L; \mathbf{k}_S, \mathbf{e}_S) = \frac{2\pi}{\hbar} r_0^2 \cdot \left|\left\langle A_S^+ A_L \right\rangle\right|^2 \cdot \tilde{S}^T(\mathbf{q}, \omega) \tag{9}$$

(the superscript T denotes temperature dependency) whereas

$$\tilde{S}^T(\mathbf{q},\omega) = \sum_{i,f} \frac{e^{-\beta E_i}}{\mathcal{Z}} |\langle f \mid \tilde{\rho}_{\mathbf{q}} \mid i\rangle|^2 \delta(E_f - E_i + \hbar\omega) \tag{10}$$

is a *generalized dynamical structure factor* (of the sample!). The partition function is denoted by $\mathcal{Z}$, and β is the inverse temperature. Now, we sum over all final states in a certain region $d\Omega\, d\omega_S$ of k-space around $\mathbf{k}_S$ and normalize to the incoming flux $\hbar c n_L$. This yields the expression

$$\frac{d^2\sigma}{d\Omega\, d\omega}(\mathbf{q},\omega) = \frac{\omega_S}{\omega_L} r_0^2 \tilde{S}^T(\mathbf{q},\omega) \tag{11}$$

for the differential cross section $d^2\sigma/d\Omega d\omega$ for a given Raman shift ω and a given momentum transfer $\mathbf{q}$. This differential cross section is proportional to the scattering volume. When performing the calculation for a scattering volume equal to unity, σ becomes the commonly used *Raman scattering efficiency*.

Finally, one can define a linear response function, the *Raman susceptibility*

$$\chi_{\mathrm{Raman}}(\mathbf{q},t) = \frac{i}{\hbar}\,\mathrm{Tr}\{\mathcal{Z}^{-1} e^{-\beta H_0}[\tilde{\rho}_{\mathbf{q}}(t), \tilde{\rho}_{-\mathbf{q}}(0)]\} \tag{12}$$

and its Fourier-transformed $\chi_{\rm Raman}(\mathbf{q},\omega)$. To relate the imaginary part of this quantity to the structure function $\tilde{S}^T(\mathbf{q},\omega)$, we use the fluctuation-dissipation theorem. The result is

$$\tilde{S}^T(\mathbf{q},\omega) = -\frac{1}{\pi}(1+n_\omega)\,\mathrm{Im}\,\chi_{\rm Raman}(\mathbf{q},\omega) \qquad (13)$$

with the Bose factor n_ω.

Equations (11) and (13) relate the Raman efficiency directly to the imaginary part of the Raman susceptibility. This evaluation of the Raman susceptibility shall be given separately, (i) in Sec. IV for the superconducting phase and Raman shifts of the order of the gap, and (ii) in Sec. V for large Raman shifts in the superconducting phase and for the normal phase.

IV. THEORY: SUPERCONDUCTING PHASE

As pointed out in Ref. 10, the Raman susceptibility due to pair-breaking and including screening is given by a polarization-like bubble made of a renormalized Raman vertex $\Lambda_{\mathbf{k}}$, a Raman vertex $\gamma_{\mathbf{k}}$, and in between two Green's function lines for Bogoliubov quasiparticles (Fig. 1a). The vertex renormalization includes corrections for Cooper-pair-producing attractive interaction as well as the repulsive Coulomb interaction, the Dyson equation for the vertex $\Lambda_{\mathbf{k}}$ in the limit $\mathbf{q}\to 0$ is given by Fig. 13 in Ref. 10.

To show more clearly the effect of screening, we write the equation for the Raman susceptibility as given in Fig. 1b and 1c. Figure 1b (with $a=\gamma_{\mathbf{k}}$ and $b=\gamma_{\mathbf{k}}$) shows the unscreened susceptibility $\chi_{\gamma\gamma}$ given by a bare polarization bubble with two Raman vertices $\gamma_{\mathbf{k}}$ and the contraction of a BCS-like ladder sum with two Raman vertices. Therefore, $\chi_{\gamma\gamma}$ includes the attractive Cooper-pair-producing interaction. We include Coulomb screening by virtue of a RPA-like sum given in Fig. 1c. The effect of screening on the electronic Raman scattering can now easily be seen.[9] If we denote by χ_{ab} a bubble, renormalized by pairing interaction, with vertices a and b at the ends as in Fig. 1b, the RPA-chain can be easily summed up (see Fig. 1c) yielding

$$\chi_{\rm Raman}(\mathbf{q}\to 0,\omega) = \chi_{\gamma\gamma}(\omega) - \frac{\chi_{\gamma 1}^2(\omega)}{\chi_{11}(\omega)}\ , \qquad (14)$$

where terms of order $\mathbf{q}^2$ have been dropped. In Eq. (14) we have used the fact that $V_{\mathbf{q}}/(1-\chi_{11}V_{\mathbf{q}})$ equals $-\chi_{11}^{-1}(1-1/\varepsilon)$, and the factor $(1-1/\varepsilon)$ is $1+O(\mathbf{q}/q_{TF})^2$.

Without taking into account Coulomb interaction, the Green's functions have a well-known massless pole (Goldstone mode) which is a consequence of the breaking of gauge symmetry in the superconducting phase.[26] Coulomb interaction makes this pole acquire a finite mass (which can be shown to correspond to the plasma frequency), so if we correctly include Coulomb screening (not done in Ref. 27) we no longer have a Goldstone mode, but a massive Anderson-Bogoliubov mode. This mode has the energy $\hbar\omega_p$ (ω_p is the plasma frequency) at the Γ point and is therefore negligible for the low energy behavior of the Raman spectra.

The susceptibilities χ_{ab} in Fig. 1b are like a ladder sum contracted with vertices $a_{\mathbf{k}}$ and $b_{\mathbf{k}}$ and can be written as a sum

$$\chi_{ab}(\mathbf{q}{=}0,\omega) = \sum_{\mathbf{k}} a_{\mathbf{k}} b_{\mathbf{k}} \lambda_{\mathbf{k}}(\omega) \qquad (15)$$

which involves the Tsuneto function[18] $\lambda_{\mathbf{k}}(\omega)$. For small values of $\mathbf{q}$ (compared to the inverse coherence length ξ and the Fermi wave vector k_F), the attractive interaction does not have to be taken into account in the summation of the ladder, and the Tsuneto function is given simply by a unmodified bubble and can be evaluated easily to be

$$\lambda_{\mathbf{k}}(\omega) = \frac{\Delta_{\mathbf{k}}^2}{E_{\mathbf{k}}^2}\tanh\left(\frac{E_{\mathbf{k}}}{2T}\right)\times \\ \times\left(\frac{1}{2E_{\mathbf{k}}+\omega+i0}+\frac{1}{2E_{\mathbf{k}}-\omega-i0}\right)\ . \qquad (16)$$

Equation (16) involves the gap function $\Delta_{\mathbf{k}}$ (which depends on the temperature) and the quasiparticle dispersion relation $E_{\mathbf{k}}^2=\xi_{\mathbf{k}}^2+\Delta_{\mathbf{k}}^2$ with $\xi_{\mathbf{k}}^2=(\epsilon_{\mathbf{k}}-\epsilon_F)^2$. The constants $\hbar$ and k_B have been set equal to 1. As already mentioned, vertex corrections due to the pairing interaction are neglected. This approximation is valid for $q\ll\xi^{-1},k_F$ (Ref. 13) and $\omega\ll\omega_p$, because the Anderson-Bogoliubov pole at the plasma frequency need no longer be included.

A first and very important fact in the expressions above is that they contain only the absolute square of the gap function, i.e. Raman scattering is *not phase sensitive*, and consequently cannot distinguish between a strongly anisotropic s gap $\left|d_{x^2-y^2}\right|$ and a $d_{x^2-y^2}$ gap.

In the preceding calculation of the unscreened correlation functions χ_{ab}, we have neglected impurity scattering as well as scattering between quasiparticles (collisionless regime). In isotropic s-wave superconductors at $T=0$ and for Raman shifts $\omega\ll 2\Delta$, it is perfectly reasonable to neglect impurity scattering, because in this regime pair breaking is not possible.[28] Also, the scattering between quasiparticles can be neglected because their density is very small for small temperatures $T\ll T_c$. For d-wave superconductors this is no longer true. The effect of impurities will be discussed in the next subsection, whereas a discussion about scattering between quasiparticles can be found in Sec. V.

The second term of (14), representing screening, vanishes if the average of $\gamma_{\mathbf{k}}\cdot\lambda_{\mathbf{k}}$ does. The Tsuneto function is fully symmetric, i.e. has A_{1g} (D_{4h} group) or A_g (D_{2h}) symmetry regardless of gap symmetry. As a consequence, the screening term vanishes unless the Raman vertex has the same symmetry as the crystal. In the tetragonal case, A_{1g}-like vertices are screened, but B_{1g}-

and B_{2g}-like are not. This is different for orthorhombic HTSC of the YBCO-type. In this case the Tsuneto function has A_1 symmetry, and the same is true for the $d_{x^2-y^2}$-like component of the mass (B_{1g} of D_{4h} group, A_g of D_{2h}). Consequently, in these orthorhombic crystals, the B_{1g} component is also screened. This discussion is also applicable to BISCO, but with interchanged roles of B_{1g} and B_{2g} modes because of the different orientation of the crystallographic unit cell with respect to the Cu-O bonds.

In tetragonal systems, the B_{1g} component of the Raman vertex has nodes at the same position as the gap function. This has severe consequences for the low-energy part of the spectra.[13] In two dimensions, the existence of the nodes of the gap function in the case of a $d_{x^2-y^2}$ gap results in a linear density of states at low energies. If the vertex has a finite value in this region, the imaginary part of the Raman susceptibility is also linear in the frequency. If the vertex has a node, however, its magnitude squared becomes quadratic with respect to the gap on the Fermi surface. This causes two additional powers of the frequency to appear, the B_{1g} component of the scattering efficiency is cubic at low frequencies.[5] Two effects can alter this behavior: an orthorhombic distortion and impurities.

In our calculations, we focus on a $d_{x^2-y^2}$-like gap function which is only a function of the direction in k-space, but not of the magnitude of $\mathbf{k}$, since the values of the gap functions sufficiently far from the Fermi surface do not affect the results. We are using the same gap function for all bands involved.

A. Effect of impurities

In contrast to scattering at non-magnetic impurities in conventional (isotropic) superconductors, the influence of impurity scattering plays an important role for superconductors with anisotropic gaps and its effect on the Raman spectrum is most pronounced for superconductors which exhibit regions in k-space where the gap almost or completely vanishes. It was shown[29,22] that in the case of d-wave pairing, impurity scattering can be described by extending the nodal points on the 2D FS to small finite regions with vanishing gap. This causes a nonvanishing density of states at the Fermi energy. For anisotropic s-wave pairing the gap anisotropy becomes smeared out leading to an increase of the minimum gap value $\Delta_{\min}$. In the case of a $\left|d_{x^2-y^2}\right|$ gap, this minimum gap increases monotonically with the impurity concentration n_i for small values of n_i.

The renormalization of the gap function by the presence of impurities causes an additional contribution, which is linear in the Raman shift ω for small Raman shifts ω, in the Raman spectra.[22] This has consequences for the B_{1g} spectrum of a *tetragonal* crystal, which, according to the theory, has a cubic ω-dependence, because a linear frequency dependence is added. As will be discussed in the next subsection, the orthorhombicity of the YBCO compounds also causes a linear addition to the cubic behavior of the B_{1g} channel spectrum.

In the case of a $\left|d_{x^2-y^2}\right|$-like, A_g symmetry gap function the impurity-induced minimal gap $\Delta_{\min}$ causes an excitation-free region to show up in the electronic Raman spectrum below a Raman shift of $2\Delta_{\min}$.

B. Effect of orthorhombic distortion

As already mentioned, orthorhombic distortions, i.e. deviations from the tetragonal symmetry, have a different effect on Y-123 and on Bi-2212. Consider the $B_{1g}\,(D_{4h})$ component of the inverse mass tensor in a *tetragonal* high-T_c superconductor with a $d_{x^2-y^2}$-like gap. The $B_{1g}\,(D_{4h})$ mass has its nodes in directions diagonal to the axes of the copper planes; the same is true for the gap function. As mentioned above, this results in the ω^3-dependence of the Raman efficiency for $B_{1g}\,(D_{4h})$ scattering, in contrast to the ω-dependence predicted for A_{1g} and B_{2g} scattering. Let us now consider the orthorhombic distortion present in Y-123. The zeros of the $B_{1g}\,(D_{4h})$ mass shift because there are no longer mirror planes through the (110) axes. For this reason, the low-energy part of the spectrum acquires a linear component in addition to the ω^3 component of the D_{4h} case.

In Bi-2212 the situation is different because the orthorhombic crystallographic cell is rotated by 45° with respect to the a- and b-axes: the orthorhombic distortion preserves the mirror planes $[a \pm b, c]$. Consequently, the B_{1g} zeros stay at the same position, the low-energy efficiency acquires no linear component.

C. Effect of multilayers

In systems with one layer of Cu-O_2 planes per unit cell there is only one sheet of Fermi surface and the mass fluctuations are essentially intraband mass fluctuations, which are very sensitive to the scattering polarizations. The scattering related to the average mass is fully screened. The simplest $A_{1g}\,(D_{4h})$ scattering is related to a Raman vertex of the form $\cos 4\phi$ symmetry while $B_{1g}\,(D_{4h})$ scattering is obtained for a $\cos 2\phi$ vertex. In multilayer systems, interband fluctuations between the various sheets FS are also important. The lowest component of such fluctuations corresponds to different *average* masses in each FS sheet. Such fluctuations do not depend on the scattering polarizations and lead to unscreened scattering of A_g symmetry.

D. Effect of sign change of $\gamma_{\mathbf{k}}$ on the Fermi surface

The behavior of the Raman vertex near the Fermi surface, especially its sign, is crucial for the scattering efficiency and, in particular, for the effect of screening. *Antiscreening*, i.e. an *enhancement* of the scattering efficiency by screening, can occur if the Raman vertex changes sign on the Fermi surface. This can be seen by considering the screening part

$$\mathrm{Im}\,\chi_{\mathrm{Scr}} = -\,\mathrm{Im}\,\frac{\chi_{\gamma 1}^2}{\chi_{11}} \tag{17}$$

of the Raman susceptibility. A positive value of $\mathrm{Im}\,\chi_{\mathrm{Scr}}$ enhances the efficiency, i.e. corresponds to antiscreening.

To show how antiscreening arises, we first write the screening term $\mathrm{Im}\,\chi_{\mathrm{scr}}$ in terms of the real and imaginary parts $\lambda' \equiv \mathrm{Re}\,\lambda$ and $\lambda'' \equiv \mathrm{Im}\,\lambda$ of the Tsuneto function and the Raman vertex γ as

$$\mathrm{Im}\,\chi_{\mathrm{Scr}} = \frac{\langle\gamma\lambda'\rangle^2\langle\lambda''\rangle - \langle\gamma\lambda''\rangle^2\langle\lambda''\rangle - 2\langle\gamma\lambda'\rangle\langle\gamma\lambda''\rangle\langle\lambda'\rangle}{\langle\lambda'\rangle^2 + \langle\lambda''\rangle^2} \ . \tag{18}$$

The imaginary part of the Tsuneto function λ'' is a positive δ-function. Consequently, the quantity $\langle\lambda''\rangle$ is a positive function of the Raman shift ω. If $\gamma_{\mathbf{k}}$ changes sign in a region around the Fermi surface, it is possible that $\langle\gamma\lambda''\rangle$ changes sign as a function of ω, i.e. has a zero. At the position of this zero, the second and the third term in the numerator of (18) vanish. The first term, $\langle\gamma\lambda'\rangle^2\langle\lambda''\rangle$, is positive and can become dominant in Eq. (18). In this case antiscreening results. In the Appendix A will be shown that antiscreening is particularly sensitive to the sign of the Raman vertex on parts of the Fermi surface around the directions of the nodes of the gap function $\Delta_{\mathbf{k}}$.

V. THEORY: NORMAL PHASE

In the normal phase, the exact mechanism which produces a finite Raman intensity almost constant over a broad frequency and temperature range, is not known. Therefore, we assume some scattering mechanism, which implies a finite lifetime of the quasiparticles. Candidates for this scattering are the quasiparticle-quasiparticle scattering in Marginal Fermi Liquid theory[20] (MFL), impurity scattering[30] or scattering due to spin fluctuations.[31] A self energy with nonvanishing imaginary part yields a susceptibility of the form

$$\chi_{ab}(\mathbf{q}{=}0,\omega) = \sum_k a_{\mathbf{k}} b_{\mathbf{k}} \nu_{\mathbf{k}}(\omega) \tag{19}$$

with the relaxation kernel (the function f' is the derivative of the Fermi function with respect to the energy)

$$\nu_{\mathbf{k}}(\omega) = -f'(\xi_{\mathbf{k}}) \frac{i\Gamma_{\mathbf{k}}}{\omega + i\Gamma_{\mathbf{k}}} \tag{20}$$

and its imaginary part

$$\mathrm{Im}\,\nu_{\mathbf{k}}(\omega) = -f'(\xi_{\mathbf{k}}) \frac{\omega\Gamma_{\mathbf{k}}}{\omega^2 + \Gamma_{\mathbf{k}}^2} \ . \tag{21}$$

This can easily be seen by evaluating a bubble with two Greens function lines for quasiparticles with an imaginary part $\Gamma_{\mathbf{k}}$ of the self energy.

Note that in the superconducting phase for Raman shifts larger than $\sim \Delta$, the relaxation effects described by (21) are also of importance. The relevant relaxation kernel in this case is

$$\nu_{\mathbf{k}}(\omega) = -f'(E_{\mathbf{k}}) \frac{\xi_{\mathbf{k}}^2}{E_{\mathbf{k}}^2} \frac{i\Gamma_{\mathbf{k}}}{\omega + i\Gamma_{\mathbf{k}}} \ , \tag{22}$$

where $\xi_{\mathbf{k}}^2 = (\epsilon_{\mathbf{k}} - \epsilon_F)^2$.

To describe the constant background in the Raman spectra in the normal phase, one has to adopt the quasiparticle scattering rate of the MFL theory[20,21]

$$\Gamma_{\mathbf{k}}(\omega) \sim \max(\alpha T, \beta\omega) \ . \tag{23}$$

In order to evaluate the real part of $\nu_{\mathbf{k}}$ using causality arguments, and to prevent divergences, we introduce a high-frequency cutoff ω_C. Note that the nearly antiferromagnetic Fermi liquid[32,33] (NAFL) and also the nested Fermi liquid[34] (NFL) yield a very similar quasiparticle scattering rate. The former can also provide a mechanism, which accounts for $d_{x^2-y^2}$ pairing. Similar results are obtained with Luttinger liquid based results.[19]

Equation (23) yields a scattering continuum which is constant for frequencies smaller than $\min(\alpha T/\beta, T)$ and for frequencies larger than the temperature T, but with different intensities. In the first case, $\Gamma_{\mathbf{k}}$ is proportional to the temperature, i.e. $\mathrm{Im}\,\chi \sim \omega/T$. Multiplying by the Bose factor $1 + n_\omega \sim T/\omega$ a constant is found. In the second case, $\Gamma_{\mathbf{k}} \sim \omega$, and, consequently, $\mathrm{Im}\,\chi = \mathrm{const}$. The Bose factor is also constant and one is left with a constant Raman intensity. Note that in the first case, $\mathrm{Im}\,\chi$ cancels the ω- and T-dependence of the Bose factor. It has been shown,[35,36,21] that $YBa_2Cu_4O_8$ does not exhibit this behavior. This has been attributed to the breakdown of MFL theory for not optimally doped cuprates.[21] Actually, in this case the spectra are nearly temperature independent *after* dividing them by the Bose factor. We shall address this question once more at the end of this section.

To discuss quasiparticle-quasiparticle (qp-qp) scattering, and its influence on electronic Raman scattering, we start with the case of a $d_{x^2-y^2}$ gap. Suppose the nodes of this gap have a width δ_0 in k-space on the Fermi surface due to impurity scattering. We use the model of Eq. (22) with a quasiparticle scattering rate $\Gamma_{\mathbf{k}}$ independent of $\mathbf{k}$ and discuss first the case $T = 0$. Then it can

be seen that the contribution of qp-qp scattering to the imaginary part of the Raman susceptibility (12) for low frequencies $\omega \ll \Delta_{\max}$ is proportional to the Drude-like factor $\omega\Gamma/(\omega^2+\Gamma^2)$ (which is, for small ω and low temperatures $T < \omega$, linear in ω if $\Gamma = \text{const}$ (semiconductors) or $\Gamma \sim \max(\omega^2, T^2)$ (FL), but constant as a function of ω if $\Gamma \sim \max(\omega, T)$ (MFL). In the tetragonal case, it is also proportional to the density of states at the Fermi surface and in the case of A_{1g} and B_{2g} polarizations to the width δ_0, and in the case of B_{1g} to the third power δ_0^3 of the width δ_0. The discussion for BISCO is analogous with the exception that B_{1g} and B_{2g} exchange their role.

Finite, but small temperatures $T \ll \Delta_{\max}$ have the effect of enlarging the widths δ_0 linearly in temperature, i.e. the temperature dependence of the contribution from qp-qp scattering is proportional to $\text{const} + T$. Note that for $T \gtrsim 0$, the Bose factor changes the linear-in-ω dependence to a constant.

For the anisotropic s gap of the form $\left|d_{x^2-y^2}\right|$ which acquires a finite minimum gap $\Delta_{\min}$ due to the presence of impurities,[22] the situation is different. The frequency dependence is also given by the factor $\omega\Gamma/(\omega^2+\Gamma^2)$ in addition to the Bose factor. But the temperature dependence is different. For temperatures $T \ll \Delta_{\min}$ smaller than the minimal gap, the density of quasiparticles is proportional to $\exp(-\Delta_{\min}/kT)$, i.e. the contribution of qp-qp scattering to the Raman efficiency is exponentially small. At $kT \approx \Delta_{\min}$, this exponential dependence on T crosses over to a power law.

The background electronic Raman spectrum in the normal phase is almost independent of temperature for nearly optimally doped high-T_c compounds only. In the overdoped and underdoped case, the materials seem to show Fermi liquid-like behavior concerning the quasiparticle scattering rate $\Gamma_{\mathbf{k}}$ (for small ω).[21,36] The temperature dependence of the scattering rate $\Gamma_{\mathbf{k}}$, as defined in (22), has been measured[37] for optimally doped and overdoped Bi-2212, and, especially in the case of the $B_{2g}\,(D_{4h})$ mode, the optimally doped sample shows $\Gamma = \alpha T$, whereas for the overdoped sample $\Gamma = \alpha' T^2 + \Gamma_0$. Therefore, the overdoped sample shows properties of a normal Fermi liquid which are predicted by theory to have $\Gamma \sim \max(\omega^2, T^2)$. The $B_{1g}\,(D_{4h})$ mode result for the optimally doped sample yields the puzzling quasiparticle scattering rate $\Gamma = \text{const}$.

VI. EXPERIMENTAL SPECTRA

The experimental determination of *absolute* Raman scattering intensities is plagued by a number of difficulties (a reason why usually "relative units" are found in the literature). The first is related to the presence of elastically scattered light in the spectra, in particular when non-ideal sample surfaces are involved. Depending on the quality of the spectrometer this leads to contributions extending typically, for the parameters of the present work, up to $50\,\text{cm}^{-1}$ from the center of the laser line. These contributions can be filtered out using a premonochromator or notch filters but, in any case, Raman scattering measurements below $50\,\text{cm}^{-1}$ remain difficult. The measurements discussed here have been performed by comparison with the known efficiency of silicon after correcting for differences in the scattering volumes. The procedure leads to errors of about 50%.

We use for comparison with the calculation the experimental data of Krantz *et al.*[6] in the case of Y-123, and Donovan *et al.*[35] in the case of Y-124. Our Figs. 4 and 5 are taken from these publications. In the case of Fig. 4 we have corrected a scale error in the abscissa found in Ref. 6. In the case of Fig. 5 we have calculated the A_{1g} component from the experimental results for the $(x'x')$ and (xy) polarizations.

The classification of the measured spectra according to irreducible representations of the symmetry group of the crystal is performed with the use of the Raman tensor $\hat{R}$ which is related to the Raman efficiency through the expression $I \sim \left|\mathbf{e}_L \hat{R} \mathbf{e}_S\right|^2$, bilinear in the Raman tensor. In the calculations, the Raman tensor does not appear explicitly, the inverse effective mass $\partial^2 E/(\partial k_i \partial k_j)$ playing its role. It is important to note that the Raman efficiency as given by the theory (Eqs. (11), (13), and (14)) is bilinear in the inverse effective mass of the Raman vertex (including the screening part!), i.e. contains the same interferences as the approach involving the Raman tensor. Note that the Tsuneto function λ is fully symmetric. In the normal phase, the scattering kernel ν has been assumed to be the same for all scattering channels.

In most of the measurements of the Raman efficiency in orthorhombic high-T_c superconductors, an A_{1g} component has been given. Strictly, this irreducible representation does not exist in D_{2h} but only in D_{4h}. In orthorhombic crystals, the Raman tensor contains two A_g components which correspond to the A_{1g} and B_{1g} components of the tetragonal D_{4h} case, and which are not distinguishable in D_{2h} because they transform in the same way. Nevertheless, quantities can be constructed in the orthorhombic case which correspond to the tetragonal A_{1g} component.

One of these is $I^{(1)} = (I_{xx} + I_{yy})/2 - I_{x'y'}$. Both, I_{xx} and I_{yy} contain A_{1g} and $B_{1g}\,(D_{4h})$, and also an interference term which cancels when I_{xx} and I_{yy} are added. The $I_{x'y'}$ efficiency contains B_{1g} and $A_{2g}\,(D_{4h})$. If we assume that the antisymmetric component (A_{2g} in D_{4h}) of the Raman tensor $\hat{R}$ vanishes (i.e. $I_{xy} = I_{yx}$), $I_{x'y'}$ corresponds to tetragonal B_{1g} and cancels the B_{1g} contribution in I_{xx} and I_{yy}. Provided that the A_{2g} component of the Raman tensor vanishes, $I^{(1)}$ corresponds to the $I_{A_{1g}}$ of the tetragonal case. Note that the antisymmetric compoment $(R_{xy} - R_{yx})/2$ of the Raman tensor vanishes in the effective mass vertex theory given in Sec. III because of $\gamma_{xy} = \gamma_{yx}$ regardless of the symmetry of the crystal, and also in the experiment in the case of tetragonal crystals but not necessarily for orthorhombic crystals. The

equality of I_{xy} and I_{yx} in the calculation is an artifact of the theory.

A second possible construction for A_{1g} is $I^{(2)} = I_{x'x'} - I_{xy}$. The $I_{x'x'}$ efficiency contains A_{1g} and B_{2g} contributions. The interference term of these two contributions vanishes in the tetragonal as well as the orthorhombic case. Both, $B_{2g}\,(D_{4h})$ and A_{2g} are contained in I_{xy}. But if the A_{2g} component of the Raman tensor vanishes, $I^{(2)}$ also corresponds to the $I_{A_{1g}}$ of the tetragonal case. In one of the experimental works[6] a different method to extract the A_{1g} component was used. Both of the expressions for $I^{(1)}$ and $I^{(2)}$ contain contributions of the $A_{2g}\,(D_{4h})$ Raman tensor component. This component may be present in the experiment, but not in the theory, a fact, that has to be kept in mind when comparing the numerical results to the measurements. Note that the Raman efficiencies in (xy) and $(x'y')$ polarization configurations also contain contributions from the antisymmetric part of the Raman tensor. In view of these uncertainties in A_{1g} we mainly focus in the next section on the directly observable components of the Raman tensor.

We shall conclude this section by taking up again the question of the validity of the effective mass approximation. In the experiment, this can be checked in two ways. First, via the dependence of the spectra on the laser frequency which should make it possible to distinguish the contributions to the Raman efficiency resulting from resonant and non-resonant transitions, respectively. The second way involves the measurement of the A_{2g} component of the mass. If the effective mass approximation is valid, the Raman vertex should be symmetric ($\gamma_{xy} = \gamma_{yx}$), i.e. the $A_{2g}\,(D_{4h})$ component should vanishes. A non-vanishing A_{2g} component of the measured scattering would cast doubts on the appropriateness of the effective mass approximation.

VII. NUMERICAL RESULTS AND DISCUSSION

To carry out the numerical BZ and FS integrations, we employed a tetrahedron approach.[38,39] The convergence of the integrations was checked by using different meshes. In Figs. 2 and 3, the results of full BZ integrations for Y-123 and Y-124, respectively, are plotted. The corresponding spectra obtained through FS integrations can be seen in Ref. 19. The Bose factor has not been included, hence the results apply to zero temperature. In both figures, the Raman shift is given in units of the gap amplitude Δ_0. Since the calculated scattering efficiencies for BZ integrations, contrary to FS integrations, are not only a function of the reduced frequency but depend also weakly on the value of Δ_0, we took for the calculations $\Delta_0 = 220\,\mathrm{cm}^{-1}$. This value of Δ_0 falls in the range of Δ_0's determined by Raman scattering and other methods. The delta-function peaks in the Tsuneto function have been broadened phenomenologically by introducing a finite imaginary part $\Gamma = 0.3\Delta_0$ of the frequency variable ω.

Figures 2 and 3 display spectra for each of the polarization configurations (yy), $(x'x')$, (xx), $(x'y')$, and (xy), as well as the symmetry component $A_{1g}\,(D_{4h})$ (defined by $I_{A_{1g}} = I_{x'x'} - I_{xy}$), the unscreened intensities, the screening part (17), and the total intensities, equal to the difference between unscreened and screening parts. Note that the $(x'y')$ configuration corresponds to the $B_{1g}\,(D_{4h})$ component because of the vanishing of the A_{2g} component in the theory.

We discuss first the results for Y-123. The A_{1g} component (in the rest of this section we use tetragonal notation unless explicitly stated) is subject to rather strong screening, however its unscreened part is comparable to that of the B_{1g} component. The relation between the unscreened and the screened (total) spectral weight of the A_{1g} component is about three. Nevertheless, the shapes of the unscreened and the screened parts are the same and, consequently, *there is almost no shift in the peak position due to screening* (contrary to the results of Ref. 5). The peak is located almost exactly at $2\Delta_0$. Note that there is no antiscreening in the A_{1g} component. The low-energy part of all A_{1g} spectra (screened and unscreened) is linear, as predicted by the theory.

As already mentioned, the $(x'y')$ component (equal to the B_{1g} component in the non-resonant case) is almost four times stronger than its screened A_{1g} counterpart. The screening is very small, its nonvanishing being an effect of the distorted tetragonality of the crystal. There is, in this case, a very small amount of antiscreening in the region below $2\Delta_0$. As in the case of the A_{1g} component, the $(x'y')$ component peaks at almost exactly the $2\Delta_0$ frequency shift. The low-frequency part has an $\alpha\omega + \beta\omega^3$ frequency dependence, the linear part arising from the distorted tetragonality, i.e. the fact that the B_{1g} mass does not vanish at exactly the same position on the Fermi surface as the gap function does.

The efficiency of the peak in the (xy) configuration (equal to the B_{2g} component in the non-resonant case) is also four or five times smaller than that of the A_{1g} peak. The (xy) peak is located at about $1.3\Delta_0$, as expected from the fact that in the neighborhood of the region where the gap is large, the B_{2g} mass vanishes. Consequently, the peak is not as sharp as in the former cases and screening vanishes since these spectra correspond to a nonsymmetric (B_{1g}) representation of the orthorhombic group (D_{2h}).

In the A_{1g} and $(x'y')$ spectra there should be a small peak at about $\omega = 2\sqrt{\epsilon_{\mathrm{vH}}^2 + \Delta_{\max}^2} \approx 3.9\Delta_0$ due to the van Hove singularity on the k_x-axis near the X point. The corresponding structure, however, is very weak, and practically invisible in Fig. 2. This is not unexpected for a 3D calculation. These peaks appear strongly when 2D calculations are performed through BZ integrations.[27]

In general, the efficiencies in Y-124 (Fig. 3) are about a factor of three less than those for its Y-123 counterpart. Moreover, the screening of the A_{1g} component of Y-123

is much stronger than that of Y-124. This may be, at least in part, due to the additional chain band: The (yy) component of Y-124 is less screened than the (yy) component of Y-123. At low frequencies, we correspondingly have antiscreening even in A_{1g}, a fact which reveals a change of sign of the effective mass on the Fermi surface (see Sec. IV D). Due to this antiscreening, the peak in the A_{1g} spectrum is shifted from $2\Delta_0$ towards approximately $1.6\Delta_0$. In contrast to the situation in Y-123, the Y-124 spectra show clearly the influence of the van Hove singularity on the spectra, as a small hump (vH) located near $2\sqrt{\epsilon_{\rm vH}^2+\Delta_{\rm max}^2} \approx 7\Delta_0$. In the A_{1g} spectrum this hump is almost screened out whereas in the $(x'y')$ spectrum it appears slightly increased by the influence of antiscreening.

To compare these predictions with the experiment let us first focus on the peak positions. The experimental results for Y-123 (Fig. 4, lower part) clearly show that the position of the (yy), $(x'x')$ and (xx) peaks is at about $300\,{\rm cm}^{-1}$, whereas the $(x'y')$ peak is located at $600\,{\rm cm}^{-1}$, i.e. at twice the frequency of the former. This fact is in sharp contrast with the calculated spectra and has been at the center of the controversy concerning the topic at hand.[40,12] It has been suggested by Devereaux *et al.*[5,12] that the B_{1g} component peaks at $2\Delta_0$, and the A_{1g} component becomes shifted down to almost Δ_0 by the screening. This interpretation contradicts our numerical results which clearly suggest that the influence of screening on the position of the A_{1g} mode is usually smaller. The frequency renormalizations of phonons around T_c also seem to contradict the interpretation in Refs. 5 and 12. It has been shown[41] that lowering the temperature of the sample in the superconducting phase causes the A_{1g} $435\,{\rm cm}^{-1}$ phonon (plane-oxygen, in-phase) to shift up in frequency and the B_{1g} (D_{4h} notation) $340\,{\rm cm}^{-1}$ phonon (plane-oxygen, out-of-phase) to shift down. This, in turn, implies an amplitude of the gap $2\Delta_0$ between $300\,{\rm cm}^{-1}$ and $360\,{\rm cm}^{-1}$ and is consistent with our interpretation of the electronic Raman spectra with the A_{1g} peak at $2\Delta_0$.

Note that the (yy), $(x'x')$ and (xx) spectra do *not* contain contributions of the A_{2g} (D_{4h}) antisymmetric component of the Raman tensor while the $(x'y')$ component does. So, the experimental results may suggest that the shift of the position of the $(x'y')$ spectrum with respect to the peak position of the other spectra is due to resonance effects. The (xy) spectrum is also influenced by the A_{2g} component. It is difficult to determine its peak position from Fig. 2, but it seems to be located at the same position as that of the (yy), $(x'x')$ and (xx) configurations. The calculation predicts it to be located at about $1.3\Delta_0$, the shift to $2\Delta_0$ can also be attributed to the existence of an A_{2g} component, like in the case of the $(x'y')$ configuration.

To compare the relative intensities of the spectra with different polarizations, we refer to Table II, which lists them together with the corresponding absolute intensities, both at the peak position. The detailed results of our FS integration have already been reported earlier.[19] We begin with Y-123 (upper panel in Table II) and compare BZ integration results to the experimental ones. With the possible exception of the A_{1g} component (and the $(x'x')$ component, which is very similar to A_{1g}), the agreement is rather good. The deviation of the A_{1g} component may be attributed to screening, which is very sensitive to sign changes and other details of the Raman vertex near the Fermi surface (such as details of the band structure and especially the exact position of the Fermi energy).

The second compound, Y-124 (lower panel in Table II), also shows reasonable agreement between the results of the BZ integration and the experiment. However, we also have problems with the A_{1g} component, as we did for Y-123.

The measured absolute intensities agree particularly well with the calculations in the case of Y-123. With the exception of A_{1g}, the discrepancy between theory and experiment is only a factor of two, which can easily be related to the difficulties in measuring absolute scattering cross sections. In the case of Y-124, the discrepancy is a bit larger, but a factor of four can still be considered good. We should also keep in mind that resonances of ω_L or ω_S with virtual interband transitions are expected to enhance the simple effective mass Raman vertex, a fact which could also explain why the measured scattering efficiencies are usually larger than the calculated ones.

We close the discussion of the numerical results with a remark about the Fermi surface integration. For Y-124, the results of the former correspond rather closely to the results from the BZ integration. The situation is different for Y-123. Here, the (xx) peak height is almost a factor four larger in the FS integration than in the BZ integration. This is likely to result from the close proximity of the van Hove singularity to the FS in the case of Y-123 (25 meV), as compared to Y-124 (110 meV).

To verify the predictions related to the effect of orthorhombic distortions as discussed in Sec. IV B, we performed a fit of the function $\alpha\omega+\beta\omega^3$ to the low-frequency part of the B_{1g} data for Y-123 reported in Ref. 6 and Ref. 42 as well as for Bi-2212 (taken from Ref. 43) and to the results of our numerical calculations for Y-123. The ratios of the cubic vs. the linear part (at $\omega = 300\,{\rm cm}^{-1}$) of the fit to the low-frequency efficiency are given in Table II.

Both measurements for Y-123 agree in their large linear part, which should be due mainly to the lack of exact tetragonality and the presence of impurities. The results of the BZ integration show a smaller linear part, because they do not take into account the influence of impurities. Finally, the result for Bi-2212 is completely different from the former results for Y-123. The linear part almost vanishes, in agreement with the preceding discussion.

VIII. CONCLUSIONS

In spite of the striking ability to predict not only general features of the observed spectra but also their peak intensities, our calculations are not able to predict the relative positions of the A_{1g} and B_{1g} peaks. According to Figs. 2 and 3 the A_{1g} spectrum should peak only slightly below $2\Delta_0$ while B_{1g} should peak at $2\Delta_0$. The experimental data of Figs. 4 and 5, however, indicate that the B_{1g} spectra peak nearly at twice the frequency of A_{1g}. Since the observed A_{1g} peak is considerably sharper than that of B_{1g}, we may want to assign the A_{1g} peak to $2\Delta_0$. Our calculations show that it is impossible to reproduce both peak frequencies with a simple gap of the form $\Delta_0 \cos 2\phi$ where ϕ is the direction of the **k**-vector. A reasonable fit was obtained in Ref. 6 with a two-dimensional FS which did not take into account the chain component and assigned *d*- and *s*-like gaps to the two bonding and antibonding sheets of the FS of the two planes in an *ad hoc* way. Within the present 3-dimensional band structure the FS cannot be broken up into bonding and antibonding plane and chain components since such sheets are interconnected at general points of *k*-space. It is nevertheless clear that there is no reason why the gap function should be the same in the various sheets for a given **k**-direction. Thus the remaining discrepancy in the peak positions between theory and experiment could be due to a more complicated $\Delta_{n\mathbf{k}}$ than a simple $\Delta_0 \cos 2\phi$ used here. Another possible source of this discrepancy is scattering through additional excitations of a type not considered here (e.g. magnetic excitations) contributing to and broadening the B_{1g} peak.

A BCS-like theory, which involves an attractive pairing potential as well as the repulsive Coulomb potential and uses an anisotropic $d_{x^2-y^2}$-like gap function in connection with the effective mass approximation used in the calculation of the absolute Raman scattering efficiencies yields result which are in significant agreement with the experimental spectra. One exception, the peak positions of the A_{1g} and the B_{1g} components, remains unexplained. The theory predicts them to be both located near $\omega = 2\Delta_0$, but the experiment shows the peak in B_{1g} at almost twice the frequency of the peak in A_{1g}. The weak B_{2g} spectrum agrees in intensity and peak position with calculations for a $d_{x^2-y^2}$-like gap. The results of other experiments, involving the temperature dependence of phonon frequencies,[41] suggest that the A_{1g} peak position corresponds to the gap amplitude $2\Delta_0$. The shifting of the B_{1g} peak towards higher frequencies may have an origin different from the mass-fluctuation-modified charge-density excitations described in the theoretical part of this paper but could also be due to a multi-sheeted gap function, more complicated than the simple $d_{x^2-y^2}$-like $\Delta_0 \cos 2\phi$ gap assumed in our calculations. The initial variation of the A_{1g} and B_{1g} scattering efficiencies vs. ω are linear as expected for that gap. The B_{1g} symmetry becomes A_g in the presence of the orthorhombic distortion related to the chains. Consequently, the scattering efficiency at low frequency is not proportional to ω^3 but should have a small linear component which is found both in the calculated and the measured spectra. In the corresponding spectrum of Bi-2212, with and orthorhombic distortion along $(x+y)$, the B_{1g} (D_{4h}) excitations also have a nonsymmetric B_{1g} (D_{2h}) orthorhombic character. Consequently, for small ω no component linear in ω is found in the measured spectra.

We have performed our calculations using either BZ or FS integration. In the case of Y-124 the spectra so obtained are very similar. For Y-123 quantitative differences appear; they are probably related to the presence of a van Hove singularity close to the FS. These singularities appear as weak structures in the calculated spectra, as expected for a 3D band structure.

ACKNOWLEDGMENTS

We thank Jens Kircher for providing us with the LMTO band structures. One of us (TS) also would like to thank his colleagues at the MPI for numerous discussions on Raman scattering and superconductors. Thanks are specially due to Igor Mazin for a critical reading of the manuscript.

APPENDIX A: ANTISCREENING AND THE SIGN OF THE RAMAN VERTEX

In Sec. IV D, we pointed out that the effect of antiscreening results from sign changes of the Raman vertex $\gamma_{\mathbf{k}}$, i.e. the inverse effective mass, on the Fermi surface. In this appendix we present a different proof using a power expansion of $\gamma_{\mathbf{k}}$.

For very low frequencies $\omega \ll \Delta_0$, only the regions around the node directions of the gap function (we assume a $d_{x^2-y^2}$-like gap) contribute to the susceptibility. We focus on a specific node of the gap function and define the point $\mathbf{k}_0$ as the point of intersection of the node line of the gap function and a specific sheet of the Fermi surface. Then we introduce an orthogonal coordinate system $\{k, k_\perp\}$ in the *a*-*b*-plane in *k*-space with the origin at $\mathbf{k}_0$, rotated in such a way that the $k_\perp$-axis is perpendicular to the node line (i.e. tangent to the Fermi surface). We write the Raman vertex as a series $\gamma(\mathbf{k}) = \sum_i \gamma_i (k_\perp/k_c)^i$ (where k_c is a cutoff), using the assumption that $\partial\gamma/\partial k = 0$. This approximation is justified since contributions to the Raman susceptibility mostly arise from a narrow region around the Fermi surface). We write Eq. (18) as

$$\mathrm{Im}\,\chi_{\mathrm{Scr}} = \sum_i \mathrm{Im}\,\chi^{(i)}_{\mathrm{Scr}}\ , \tag{A1}$$

whereas $\mathrm{Im}\,\chi^{(i)}_{\mathrm{Scr}}$ contains i-th powers in $k_\perp$ from the expansion of $\gamma_{\mathbf{k}}$. The first three terms in this sum are

$$\begin{aligned}
\mathrm{Im}\,\chi^{(0)}_{\mathrm{Scr}} &= -\gamma_0^2\langle\lambda''\rangle \\
\mathrm{Im}\,\chi^{(1)}_{\mathrm{Scr}} &= -2\gamma_0\gamma_1\langle k_\perp\lambda''\rangle \\
\mathrm{Im}\,\chi^{(2)}_{\mathrm{Scr}} &= -2\gamma_0\gamma_2\langle k_\perp^2\lambda''\rangle \\
&-\gamma_1^2\frac{\langle\lambda''\rangle(\langle k_\perp\lambda''\rangle^2-\langle k_\perp\lambda'\rangle^2)+2\langle\lambda'\rangle\langle k_\perp\lambda'\rangle\langle k_\perp\lambda''\rangle}{\langle\lambda'\rangle^2+\langle\lambda''\rangle^2}\ .
\end{aligned} \tag{A2}$$

Now we investigate the behavior of $\langle k_\perp^i\lambda''\rangle$ in the low frequency limit. We set $v_F=1$ and $\Delta_0=1$ (this represents a simple change in scales). Then, $E_{\mathbf{k}}=k$ ($E_{\mathbf{k}}$ is constant as function of $k_\perp$ by definition), $\Delta_{\mathbf{k}}=k_\perp$, and therefore $\Delta_{\mathbf{k}}^2/E_{\mathbf{k}}^2=k_\perp^2/k^2$ and $\lambda''\sim(k_\perp/k)^2\cdot\delta(2k-\omega)$ from Eq. (16). We perform a 2D BZ integration which has to be cut off at a value proportional to ω in the $k_\perp$ integration and find

$$\begin{aligned}
\langle k_\perp^i\lambda''\rangle &\sim \int dk_\perp\,dk\,k_\perp^i\cdot\frac{k_\perp^2}{k^2}\delta(2k-\omega) \\
&\sim \omega^{-2}\int^\omega dk_\perp\,k_\perp^{i+2}\sim\omega^{i+1}
\end{aligned} \tag{A3}$$

as the low frequency behavior. The same is true for the real part $\langle k_\perp^i\lambda'\rangle$. Note that the proportionality constant in ($A3$) is positive. This implies that $\mathrm{Im}\,\chi^{(i)}_{\mathrm{Scr}}\sim\omega^{i+1}$ and

$$\begin{aligned}
\mathrm{Im}\,\chi_{\mathrm{Scr}} = -\big(&\alpha_0\gamma_0^2\omega+\alpha_1\gamma_0\gamma_2\omega^2+(\alpha_2\gamma_0\gamma_2+\alpha_3\gamma_1^2)\omega^3 \\
&+O(\omega^4)\big)
\end{aligned} \tag{A4}$$

with positive constants α_0, α_1 and α_2. The sign of α_3 depends on the specific case.

For a tetragonal Fermi surface, we only have to focus on the A_{1g} mode because the screening contributions to the other components vanish by symmetry. The A_{1g} symmetry implies $\gamma_1=0$ because of the σ_d symmetry operation (reflection at ΓS) which transforms $\gamma_1 k_\perp\to-\gamma_1 k_\perp$. Then, the screening term for low frequencies can be written as

$$\mathrm{Im}\,\chi_{\mathrm{Scr}} = -\left(\alpha_0\gamma_0^2\omega+\alpha_2\gamma_0\gamma_2\omega^3+\cdots\right)\ . \tag{A5}$$

If there are nodes in the Raman vertex near the node of the gap function, then $\gamma_0\gamma_2<0$, i.e. the screening term is negative for very small ω, but eventually crosses zero because of the ω^3 contribution. For large $\omega\gtrsim 2\Delta_0$, the approximation $\langle\gamma\lambda\rangle\approx\langle\gamma\rangle\langle\lambda\rangle$ yields $\chi_{\mathrm{Scr}}=-\langle\gamma\rangle^2\chi_{11}$, which is the screening term for an isotropic Fermi surface with a scalar Raman vertex $\langle\gamma\rangle$, and therefore negative. If the Raman vertex does not show nodes near the node of the gap function, $\gamma_0\gamma_2$ is larger than zero, and the screening term is not likely to change sign.

In the orthorhombic case of a weakly distorted tetragonality, the B_{1g} (D_{4h}) zero in the Raman vertex may shift with respect to the gap node. This can be described by a small $\gamma_0\neq0$ and $\gamma_1\neq0$; γ_2 can be neglected. The low frequency screening term then has the form

$$\mathrm{Im}\,\chi_{\mathrm{Scr}} = -\left(\alpha_0\gamma_0^2\omega+\alpha_1\gamma_0\gamma_1\omega^2+\alpha_3\gamma_1^2\omega^3\cdots\right)\ . \tag{A6}$$

The first an the third term have almost A_{1g} symmetry whereas the second term has almost B_{1g} (D_{4h}) symmetry. It can be shown that the term proportional to ω^2 vanishes if the other nodes of the gap function are taken into account. Whether antiscreening exists or not depends on the sign of α_3.

It can be seen that for small values of γ_0, the antiscreening can start already at very small Raman shifts as is the case in the calculations, Fig. 3, B_{1g} panel.

[1] J. G. Bednorz and K. A. Müller, Z. Phys. B **64**, 189 (1986).
[2] K. B. Lyons, S. H. Liou, M. Hong, H. S. Chen, J. Kwo, and T. J. Negron, Phys. Rev. B **36**, 5592 (1987).
[3] R. C. Dynes, Solid State Commun. **92**, 53 (1994).
[4] J. R. Schrieffer, Solid State Commun. **92**, 129 (1994).
[5] T. P. Devereaux, D. Einzel, B. Stadlober, R. Hackl, D. H. Leach, and J. J. Neumeier, Phys. Rev. Lett. **72**, 396 (1994).
[6] M. Krantz and M. Cardona, J. Low Temp. Phys. **99**, 205 (1995).
[7] C. Thomsen and M. Cardona, in: *Phys. Prop. of High Temp. Superconductors I*, ed. D. M. Ginsberg, p. 409.
[8] A. A. Abrikosov and L. A. Fal'kovskiĭ, Sov. Phys. JETP **13**, 179 (1961).
[9] A. A. Abrikosov and V. M. Genkin, Sov. Phys. JETP **38**, 417 (1974).
[10] M. V. Klein and S. B. Dierker, Phys. Rev. B **29**, 4976 (1984).
[11] P. B. Allen, Phys. Rev. B **13**, 1416 (1976).
[12] T. P. Devereaux, D. Einzel, B. Stadlober, and R. Hackl, Phys. Rev. Lett. **72**, 3291 (1995).
[13] T. P. Devereaux and D. Einzel, Phys. Rev. B **51**, 16336 (1995).
[14] M. Krantz, I. I. Mazin, D. H. Leach, W. Y. Lee, and M. Cardona, Phys. Rev. B **51**, 5949 (1995).
[15] W. Kohn and L. J. Sham, Phys. Rev. **140**, A1133 (1965).
[16] O. K. Andersen, O. Jepsen, A. I. Liechtenstein, and I. I. Mazin, Phys. Rev. B **49**, 4145 (1994).
[17] O. K. Andersen, A. I. Liechtenstein, C. O. Rodriguez, I. I. Mazin, O. Jepsen, V. P. Antropov, O. Gunnarson, and S. Gopalan, Physica C **185-189**, 147 (1991).
[18] T. Tsuneto, Phys. Rev. **118**, 1029 (1960).
[19] M. Cardona, T. Strohm, and J. Kircher, in: *Spectroscopic Studies of Superconductors*, ed. I. Bozovic, Proc. SPIE **2696**, 182 (1996).
[20] C. M. Varma, P. B. Littlewood, S. Schmitt-Rink, E. Abrahams, and A. E. Ruckenstein, Phys. Rev. Lett. **63**, 1996 (1989).
[21] C. M. Varma, Phys. Rev. Lett. **75**, 898 (1995).
[22] T. P. Devereaux, Phys. Rev. Lett. **21**, 4313 (1995).
[23] O. K. Andersen, Phys. Rev. B **12**, 3060 (1975).
[24] V. N. Kostur, Z. Phys. B **89**, 149 (1992).
[25] P. Wölfle, J. Low Temp. Phys. **22**, 157 (1976).
[26] P. W. Anderson, Phys. Rev. **112**, 1900 (1958).
[27] D. Branch and J. P. Carbotte, Phys. Rev. B **52**, 603 (1995).

[28] P. W. Anderson, Phys. Rev. Lett. **3**, 328 (1959).
[29] L. S. Borkowski and P. J. Hirschfeld, Phys. Rev. B **49**, 15404 (1994).
[30] P. J. Hirschfeld, P. Wölfle, and D. Einzel, Phys. Rev. B **37**, 83 (1988).
[31] S. M. Quinlan, P. J. Hirschfeld, and D. J. Scalapino, Phys. Rev. B **53**, 8575 (1996).
[32] A. J. Millis, H. Monien, and D. Pines, Phys. Rev. B **42**, 167 (1990).
[33] V. Barzykin and D. Pines, Phys. Rev. B **52**, 13585 (1995).
[34] J. Ruvalds and A. Virosztek, Phys. Rev. B **43**, 5498 (1991).
[35] S. Donovan, J. Kircher, J. Karpinski, E. Kaldis, and M. Cardona, J. Supercond. **8**, 417 (1995).
[36] T. Zhou, K. Syassen, M. Cardona, J. Karpinski, and E. Kaldis, Solid State Comm. **99**, 669 (1996).
[37] R. Hackl, G. Krug, R. Nemetschek, M. Opel, and B. Stadlober, in: *Spectroscopic Studies of Superconductors*, ed. I. Bozovic, Proc. SPIE **2696**, 194 (1996).
[38] G. Lehmann and M. Tant, Phys. Status Solidi B **54**, 469 (1972).
[39] O. Jepsen and O. K. Andersen, Solid State Commun. **9**, 1793 (1971).
[40] M. Krantz and M. Cardona, Phys. Rev. Lett. **72**, 3290 (1995).
[41] B. Friedl, C. Thomsen, and M. Cardona, Phys. Rev. Lett. **65**, 915 (1990).
[42] R. Hackl, W. Gläser, P. Müller, D. Einzel, and K. Andres, Phys. Rev. B **38**, 7133 (1988).
[43] T. Staufer, R. Nemetschek, R. Hackl, P. Müller, and H. Veith, Phys. Rev. Lett. **68**, 1069 (1992).

TABLE I. The ratio between the linear and cubic parts of the low energy Raman efficiency in B_{1g} (D_{4h}) configuration of several high-T_c compounds at a Raman shift of $\omega = 300\,\mathrm{cm}^{-1}$.

HTSC	cubic:linear in B_{1g}	Reference
Y-123	1	Krantz *et al.*[6]
Y-123	1	Hackl *et al.*[42]
Y-123	0.35	BZ integration
Bi-2212	0.07	Staufer *et al.*[43]

TABLE II. Comparison of the experimental peak scattering efficiencies given in units of $10^{-8}\,\mathrm{cm\,cm^{-1}\,sr^{-1}}$ to the theoretical predictions (from Fermi surface integrations, Ref. 19, as well as Brillouin zone integrations, present work) for Y-123 and Y-124.

Y-123	FS integration[19]		BZ integration		Experiment[6]	
Polarization	absolute	relative	absolute	relative	absolute	relative
yy	20.0	1.00	19.6	1.00	40	1.00
xx	28.0	1.40	7.2	0.37	19	0.48
xy	3.0	0.15	2.5	0.13	4	0.10
$x'x'$			5.0	0.26	26	0.65
$x'y'$	4.8	0.24	10.6	0.54	12	0.30
A_{1g}	19.2	0.96	3.0	0.15	18	0.45

Y-124	FS integration[19]		BZ integration		Experiment[35]	
Polarization	absolute	relative	absolute	relative	absolute	relative
yy	6.3	1.00	4.4	1.00	18.0	1.00
xx	1.5	0.24	1.4	0.32	7.2	0.40
xy	1.1	0.17	0.5	0.11	2.6	0.14
$x'x'$			1.4	0.32	12.0	0.66
$x'y'$	2.8	0.44	2.3	0.52	5.6	0.31
A_{1g}	1.1	0.17	1.0	0.23	6.9	0.38

FIG. 1. Incorporation of screening effects into the theory of Raman scattering by electronic excitations in HTSC. The grey shaded bubbles are sums of ladders contracted with vertices a and b. Wavy lines correspond to the long-range Coulomb interaction, dashed lines to the attractive pairing interaction. The equation on the last line corresponds to Eq. (14).

FIG. 2. Results from the BZ integration for Y-123. Given in the five panels are absolute efficiencies for electronic Raman scattering. The upper three curves are labelled using the irreducible representation (D_{4h}) of the scattering mass, the lower two panels with the polarization geometry. Each of the five panels contains the total absolute Raman efficiency according to Eq. (11) and (13) and its two constituents, the unscreened and the screening part according to Eq. (14).

FIG. 3. Results from the Brillouin zone integration for Y-124. For details see the caption of Fig. 2.

FIG. 4. Experimental Raman scattering efficiencies for Y-123 from Ref. 6. The vertical scales are absolute Raman efficiencies, measured at $T = 10\,\mathrm{K}$ and an exciting laser wavelength of $\lambda = 488\,\mathrm{nm}$ (Note that a scale error found in Ref. 6 has been corrected). The A_{1g} component extracted according to $I_{A_{1g}} = (I_{xx} + I_{yy})/2 - I_{x'y'}$ is plotted in the lower panel together with the quasitetragonal B_{1g} and B_{2g} components.

FIG. 5. Upper panel: experimental absolute Raman efficiencies given for the five specified polarization configurations for Y-124 from Ref. 35. These data are taken at $T = 10\,\mathrm{K}$ with an exciting laser wavelength of $\lambda = 514.5\,\mathrm{nm}$. Lower panel: smoothed curves and the A_{1g} spectrum additionally extracted from the former. In both panels, consecutive offsets of $0, 1, \ldots, 4 \times 2.5\,\mathrm{cm^{-1}sr^{-1}cm}$ were used.

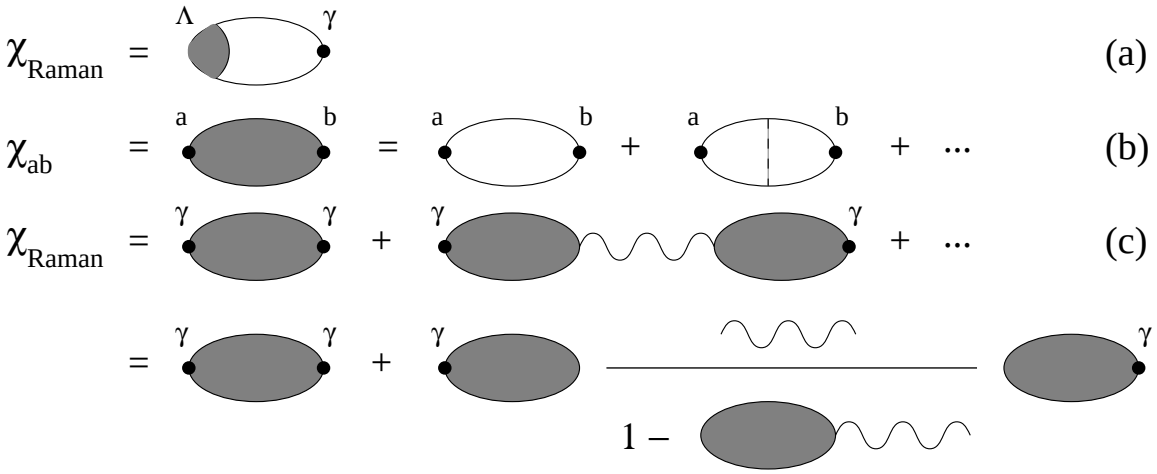

Figure 1

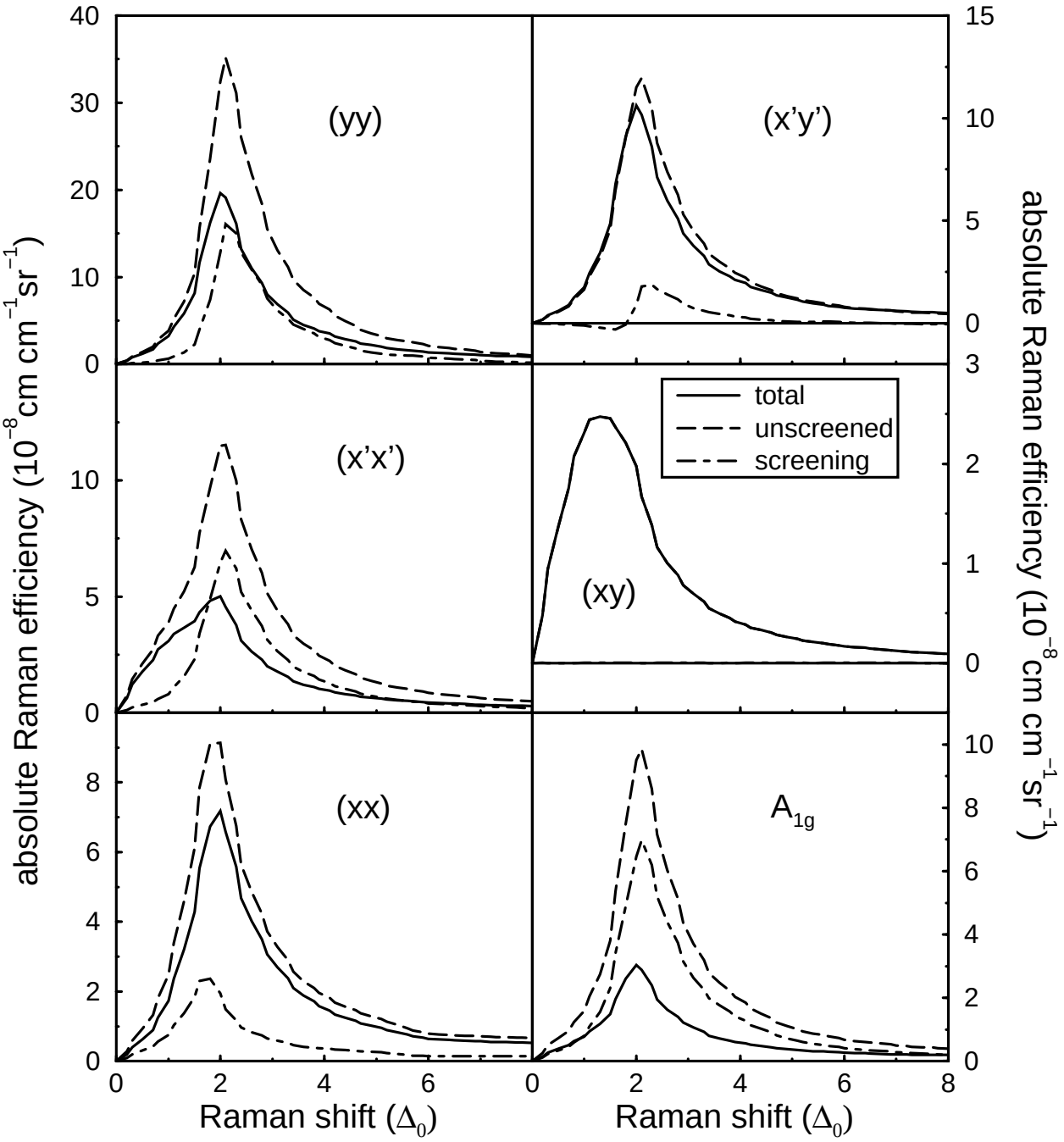
Y−123
(yy)
(x'y')
(x'x')
(xy)
(xx)
A1g
total
unscreened
screening
absolute Raman efficiency (10−8 cm cm−1 sr−1)
absolute Raman efficiency (10−8 cm cm−1 sr−1)
Raman shift (Δ0)
Raman shift (Δ0)

Figure 2

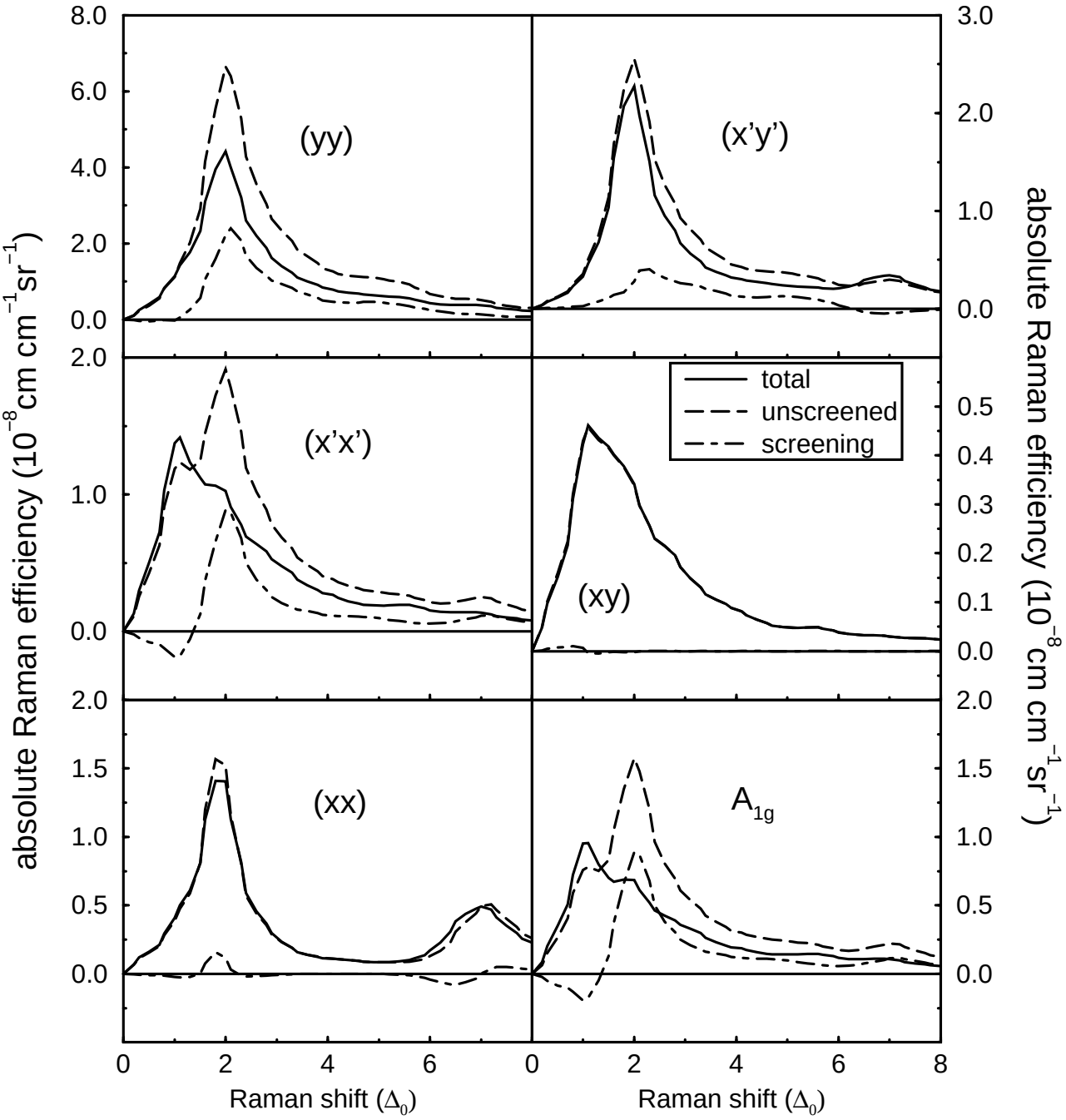
Y−124
(yy)
(x'y')
(x'x')
(xy)
(xx)
A1g
total
unscreened
screening
absolute Raman efficiency (10−8 cm cm−1 sr−1)
absolute Raman efficiency (10−8 cm cm−1 sr−1)
Raman shift (Δ0)
Raman shift (Δ0)

Figure 3

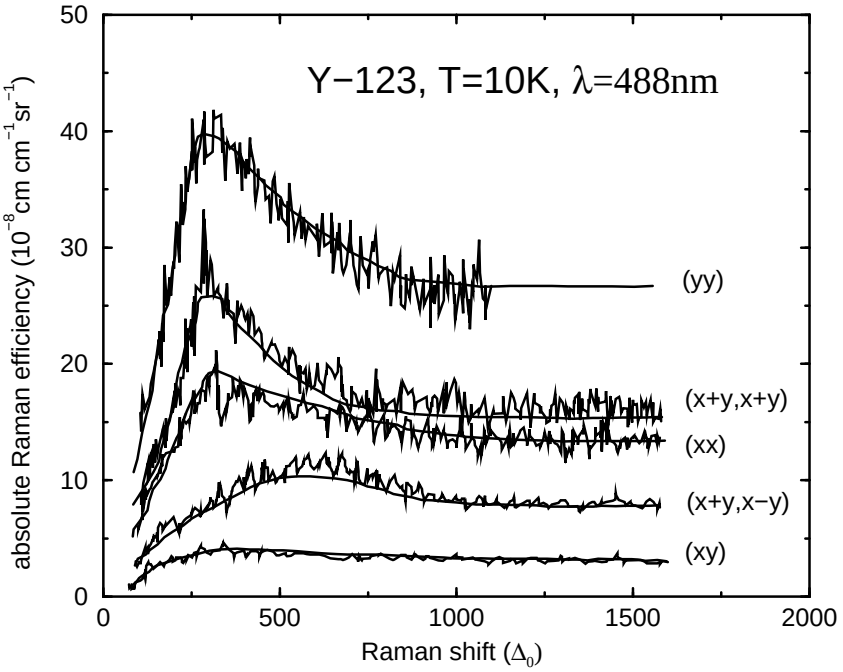
Y−123, T=10K, λ=488nm
absolute Raman efficiency (10^{-8}cm cm^{-1}sr^{-1})
Raman shift (Δ_0)
(yy)
(x+y,x+y)
(xx)
(x+y,x−y)
(xy)
0
10
20
30
40
50
0
500
1000
1500
2000

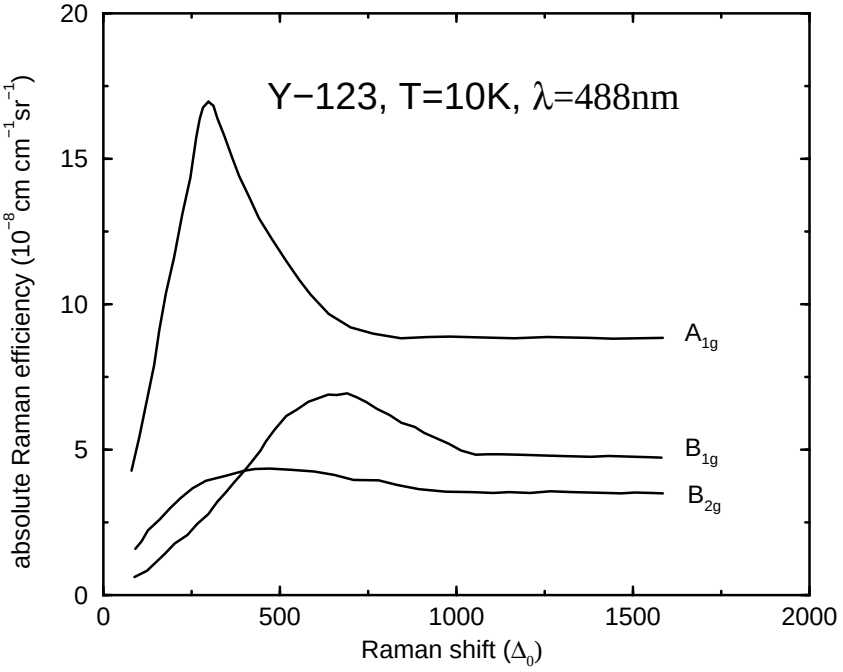
Y−123, T=10K, λ=488nm
absolute Raman efficiency (10^{-8}cm cm^{-1}sr^{-1})
Raman shift (Δ_0)
A_{1g}
B_{1g}
B_{2g}
0
5
10
15
20
0
500
1000
1500
2000

Figure 4

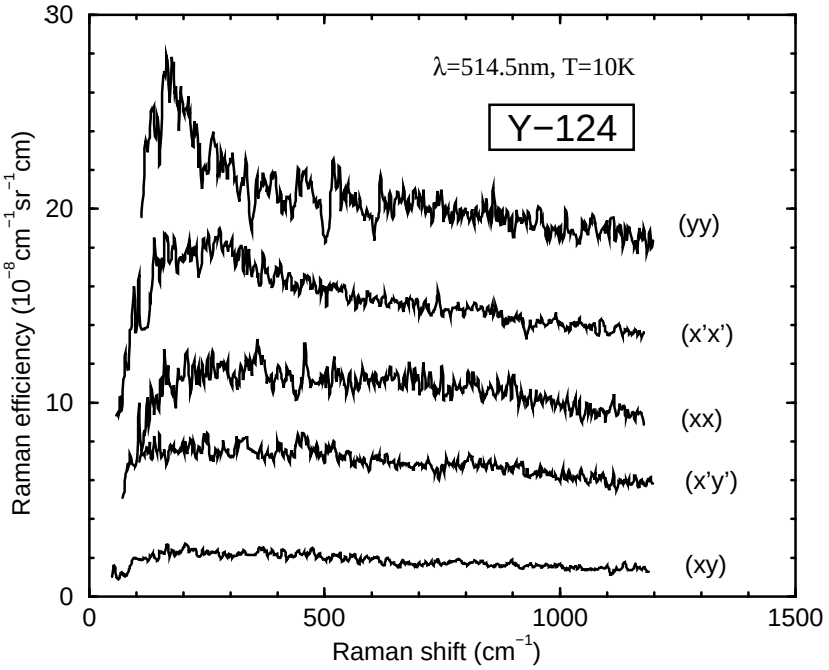
λ=514.5nm, T=10K
Y−124
(yy)
(x'x')
(xx)
(x'y')
(xy)
Raman efficiency (10^-8 cm^-1 sr^-1 cm)
Raman shift (cm^-1)
0
10
20
30
0
500
1000
1500

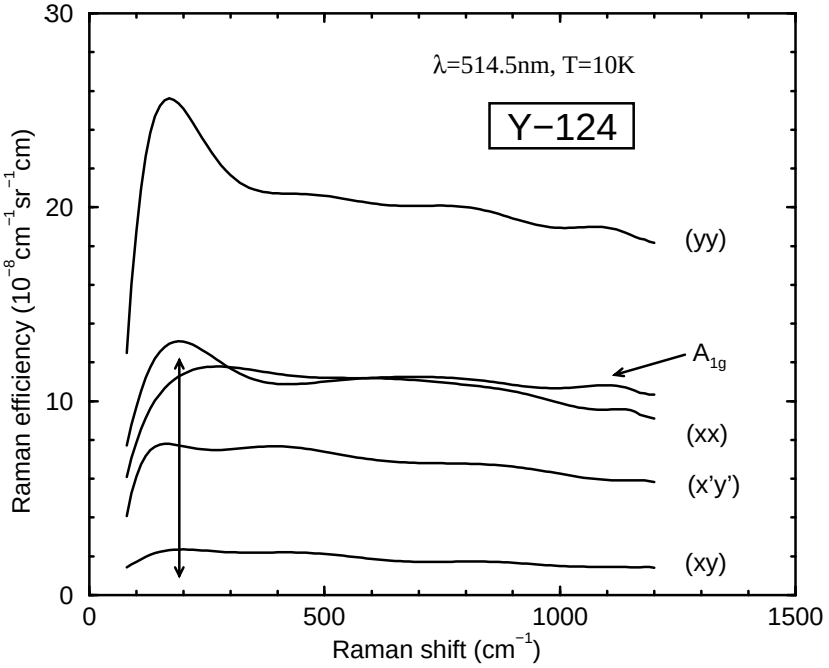
λ=514.5nm, T=10K
Y−124
(yy)
A1g
(xx)
(x'y')
(xy)
Raman efficiency (10^-8 cm^-1 sr^-1 cm)
Raman shift (cm^-1)
0
10
20
30
0
500
1000
1500

Figure 5